Structural Evidence for Enhancement of Sequential Vitamin D₃ Hydroxylation Activities by Directed Evolution of Cytochrome P450 Vitamin D₃ Hydroxylase*[S]

Yoshiaki Yasutake[‡], Yoshikazu Fujii[§¶], Taiki Nishioka[§], Woo-Kwang Cheon[‡1], Akira Arisawa[¶], and Tomohiro Tamura[‡§2]

From the [‡]Bioproduction Research Institute, National Institute of Advanced Industrial Science and Technology (AIST), Sapporo 062-8517, the [§]Laboratory of Molecular Environmental Microbiology, Graduate School of Agriculture, Hokkaido University, Sapporo 060-8589, and [¶]Bioresource Laboratories, Mercian Corporation, Shizuoka 438-0078, Japan

Vitamin D₃ hydroxylase (Vdh) isolated from actinomycete *Pseudonocardia autotrophica* is a cytochrome P450 (CYP) responsible for the biocatalytic conversion of vitamin D₃ (VD₃) to 1α,25-dihydroxyvitamin D₃ (1α,25(OH)₂VD₃) by *P. autotrophica*. Although its biological function is unclear, Vdh is capable of catalyzing the two-step hydroxylation of VD₃, i.e. the conversion of VD₃ to 25-hydroxyvitamin D₃ (25(OH)VD₃) and then of 25(OH)VD₃ to 1α,25(OH)₂VD₃, a hormonal form of VD₃. Here we describe the crystal structures of wild-type Vdh (Vdh-WT) in the substrate-free form and of the highly active quadruple mutant (Vdh-K1) generated by directed evolution in the substrate-free, VD₃-bound, and 25(OH)VD₃-bound forms. Vdh-WT exhibits an open conformation with the distal heme pocket exposed to the solvent both in the presence and absence of a substrate, whereas Vdh-K1 exhibits a closed conformation in both the substrate-free and substrate-bound forms. The results suggest that the conformational equilibrium was largely shifted toward the closed conformation by four amino acid substitutions scattered throughout the molecule. The substrate-bound structure of Vdh-K1 accommodates both VD₃ and 25(OH)VD₃ but in an anti-parallel orientation. The occurrence of the two secosteroid binding modes accounts for the regioselective sequential VD₃ hydroxylation activities. Moreover, these structures determined before and after directed evolution, together with biochemical and spectroscopic data, provide insights into how directed evolution has worked for significant enhancement of both the VD₃ 25-hydroxylase and 25(OH)VD₃ 1α-hydroxylase activities.

[1] Present address: Dept. of Physical Education, College of Physical Education, Keimyung University, 2800 Dalgubeoldaero, Dalseo-gu, Daegu 704-701, South Korea.
[2] To whom correspondence should be addressed: Bioproduction Research Institute, National Institute of Advanced Industrial Science and Technology (AIST), 2-17-2-1, Tsukisamu-Higashi, Toyohira, Sapporo 062-8517, Japan. Tel.: 81-11-857-8938; Fax: 81-11-857-8980; E-mail: t-tamura@aist.go.jp.

Vitamin D₃ (VD₃)[3] is a B-ring opening secosteroid involved in a wide variety of biological functions in mammals (1). In humans, VD₃ is converted into its physiologically active form, 1α,25-dihydroxyvitamin D₃ (1α,25(OH)₂VD₃), via hydroxylation reactions that are catalyzed by several cytochrome P450s (CYPs) (1, 2). The first hydroxylation is done at the C25 position of VD₃ by CYP27A1 (2, 3) and CYP2R1 (2, 4) in the liver to produce 25-hydroxyvitamin D₃ (25(OH)VD₃). The second proceeds at the C1α position of 25(OH)VD₃ by CYP27B1 in the kidney (5) (Fig. 1). The final product, 1α,25(OH)₂VD₃, functions as a hormone with a critical role in maintaining calcium and phosphate homeostasis as well as in controlling the differentiation and proliferation of multiple cell types (1, 2, 6). Indeed, the many symptoms associated with VD₃ deficiency and the VD metabolic disorder, which include psoriasis, osteoporosis, rickets, and hypoparathyroidism, are treated using 1α,25(OH)₂VD₃ and its derivatives (1).

Although the chemical synthesis of 1α,25(OH)₂VD₃ from cholesterol is an established method, it is inefficient, the maximum yield is no more than 1% (7). Alternatively, biocatalytic conversion by the actinomycete *Pseudonocardia autotrophica* is currently in practical use for the industrial production of 1α,25(OH)₂VD₃ (8, 9). We have recently cloned the gene encoding the VD₃ hydroxylating enzyme (Vdh) of *P. autotrophica*, showing that Vdh is a CYP with ~43% amino acid sequence similarities with the members of the CYP107 family (10). There were two more interesting findings of this study. First, we found that Vdh is capable of catalyzing regio- and stereoselective sequential hydroxylations at the C25 and C1α positions of VD₃. An *in vitro* assay using a recombinant enzyme revealed that Vdh clearly exhibits VD₃ 25-hydroxylase and 25(OH)VD₃ 1α-hydroxylase activities (Fig. 1). These enzymatic properties are consistent with phenomena in the course of biotransformation: the 25(OH)VD₃ level initially increases, followed by a gradual increase in the 1α,25(OH)₂VD₃ level in culture media. No 1α-hydroxyvitamin D₃ was detected in either *in vivo* or *in vitro* experiments. Second, the VD₃ 25-hydroxylase activity of Vdh is comparable with that of physiologically VD₃-
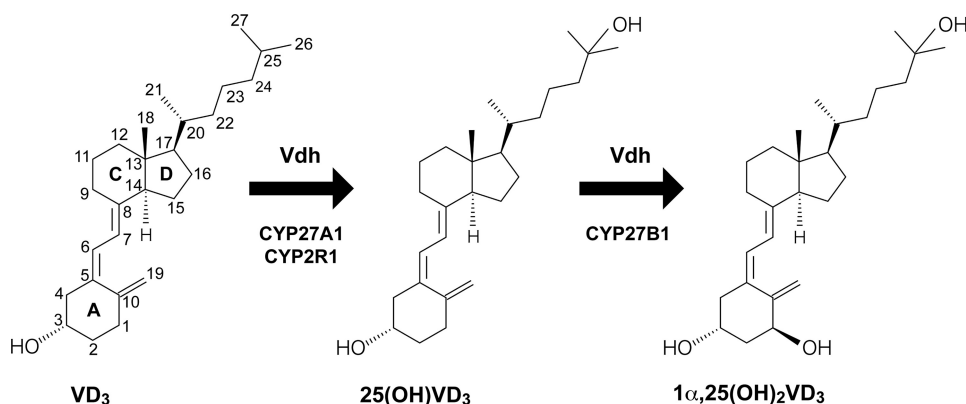
FIGURE 1. Scheme of catalytic conversion of VD$_3$ to 1α,25(OH)$_2$VD$_3$. In humans, VD$_3$ is physiologically activated mainly by CYP27A1, CYP2R1, and CYP27B1 in the liver and kidney. Vdh from *P. autotrophica* also catalyzes the conversion of VD$_3$ to 1α,25(OH)$_2$VD$_3$ by regio- and stereoselective sequential hydroxylations.

metabolizing CYP27A1 (2, 3) and CYP2R1 (2, 4) despite the fact that VD$_3$ is probably a nonnative substrate for Vdh.

CYPs are hemoproteins found across almost all of the Trees of Life and have extremely diverse biological functions, including biosynthesis of steroid hormones, lipids, and complex antibiotics, such as polyketides, detoxification of xenobiotics, drug metabolism, and bioconversion of recalcitrant molecules into usable carbon sources (11). A typical reaction catalyzed by CYPs is hydroxylation (monooxygenation), although several CYPs catalyze even more complex reactions such as epoxidation, C-C bond coupling and cleavage, and dehalogenation. This intriguing functional diversity of CYPs has led to many studies on their three-dimensional structures, which attempt to understand the structural mechanism of substrate recognition, interactions with redox partner proteins, electron and proton transfer, and catalytic reactions (12). Additionally, the versatility of CYPs is highly attractive for their potential uses as biocatalysts in chemical and pharmaceutical applications. Furthermore, protein engineering has been applied to improve and specialize the function of CYPs from bacteria and mammals (13–18). To realize more effective bioconversion of VD$_3$, biotransformation activity from VD$_3$ to 25(OH)VD$_3$ was improved by a combination of random and site-saturated mutagenesis, and finally, a highly active Vdh mutant (Vdh-K1) was obtained (10). Vdh-K1 is a quadruple mutant (T70R/V156L/E216M/E384R) that is ~22 times more active in the hydroxylation of VD$_3$ to 25(OH)VD$_3$ than wild-type Vdh (Vdh-WT) in *in vivo* bioconversion using *Escherichia coli* cells (10). Intriguingly, the four mutational points do not lie in the substrate-binding pocket, but are scattered throughout the molecule. Thus, it is of considerable interest as to how these mutations effect the significant enhancement in Vdh activity and how the enzyme recognizes each substrate.

Here we report the crystal structures of Vdh-WT and Vdh-K1 in the presence and absence of VD$_3$/25(OH)VD$_3$. The directed evolution and the x-ray structures show the importance of the conformational transition from open to closed states rather than the local active-site structure for activity enhancement. Furthermore, the VD$_3$- and 25(OH)VD$_3$-bound Vdh-K1 structures shed light on the occurrence of two antiparallel substrate-binding modes, reliably enabling regioselective sequential hydroxylation of VD$_3$.

EXPERIMENTAL PROCEDURES

Materials—All enzymes used for genetic manipulation were purchased from New England Biolabs, Takara, Promega, and Stratagene. Spinach ferredoxin and ferredoxin reductase used for enzyme assay were purchased from Sigma. 25(OH)VD$_3$ was kindly provided by Mercian Co. Ltd. Partially methylated β-cyclodextrin (PMβCD) was purchased from Junsei Chemical Inc. All other chemicals were purchased from Sigma or WAKO Pure Chemicals Inc.

Protein Expression and Purification—The recombinant proteins used in this work contained a His$_6$ tag at the C terminus. Overproduction of Vdh-WT was carried out using a *Rhodococcus erythropolis* expression system (19) or *E. coli*, and purified by Ni-affinity chromatography and anion exchange chromatography, as previously described (10, 20). The highly active Vdh-K1 mutant (T70R/V156L/E216M/E384R) was generated by directed evolution (10). Recombinant Vdh-K1 was produced using pET22b expression vector (Novagen) in *E. coli* strain BL21(DE3). Overexpression was induced by the addition of 0.1 mM isopropyl β-D-thiogalactoside for 20 h at 22 °C in Luria-Bertani (LB) medium supplemented with 100 μM FeSO$_4$ and 80 μg/ml of 5-aminolevurinic acid. The cells were harvested and resuspended in buffer A (50 mM Tris-HCl, pH 7.5, and 10% glycerol) supplemented with 2 mM dithiothreitol (DTT). The cells were lysed by sonication, and the homogenate was clarified by centrifugation. The supernatant was dialyzed against buffer A, and then applied to a Ni-affinity column (HIS-SELECT resin; Sigma) pre-equilibrated with buffer A. The column was washed with buffer A, and the enzyme was eluted with a linear gradient of 0–400 mM imidazole in buffer A. The red fractions were collected, dialyzed against buffer B (20 mM Tris-HCl, pH 7.5, 10% glycerol, 1 mM DTT, and 0.5 mM EDTA), and subsequently applied to a DEAE-Sephacel anion-exchange column (GE Healthcare) pre-equilibrated with buffer B. The enzyme was eluted with a linear gradient of 0–400 mM NaCl in buffer B. The individual fractions were analyzed by SDS-PAGE. A carbon monoxide difference spectral assay was performed to verify the Vdh concentration (21). Vdh single mutants (T70R, V156L, E216M, and E384R) were also prepared using inverse PCR (22) with appropriate synthetic oligonucleotides as primers and pET29-Vdh-WT (10) as the template. Each mutant was expressed by *E. coli* BL21(DE3) and purified with the same procedure as for Vdh-K1.

UV-visible Spectral Measurements—The substrate-induced spectral shift was monitored using a JASCO V-630 biospectrophotometer with 1-cm path length quartz cells. VD$_3$ and 25(OH)VD$_3$ were dissolved in dimethyl sulfoxide at concentrations ranging from 50 μM to 2 mM, and 10 μl of the substrate solution was added to 990 μl of reaction mixture containing 2.5 μM Vdh-WT or Vdh mutants, 20 mM Tris-HCl, pH 7.5, and 0.05% PMβCD or 0.02% γ-cyclodextrin (γCD). PMβCD and

γCD were used to increase the water solubility of VD$_3$ and 25(OH)VD$_3$, respectively (9, 23). CD concentrations referred to those adopted in actual VD$_3$ bioconversion by *P. autotrophica*. The correct K_d values cannot be determined due to the low substrate solubility and the presence of inclusion complex of substrate and CD.

Enzyme Activity Measurements—VD$_3$ 25-hydroxylase and 25(OH)VD$_3$ 1α-hydroxylase activities were measured by reconstitution experiments. One milliliter of reaction mixture containing 500 nM Vdh-WT or 100 nM Vdh-K1, 81.4 mM Tris-HCl, pH 7.5, 100 mM NaCl, 96 μg/ml of spinach ferredoxin, 0.1 units/ml of spinach ferredoxin reductase, 3 units/ml of glucose dehydrogenase, 2 mM NADH, 2 mM NADPH, 60 mM D-glucose, 1% dimethyl sulfoxide, and 30 μM VD$_3$ or 25(OH)VD$_3$ was used for enzyme activity measurements. Enzymatic reaction was initiated by the addition of NAD(P)H, followed by incubation at 30 °C. Aliquots of the reaction mixture were collected after 20 (Vdh-WT) or 5 min (Vdh-K1), and extracted once with 1.5 ml and once with 0.75 ml of ethyl acetate. The combined ethyl acetate phase was allowed to dry, and the resulting residue was dissolved in 200 μl of methanol. The methanol solution was analyzed by a high-performance liquid chromatography (HPLC) apparatus equipped with a J'sphere ODS-H80 (I.D. 4.6 × 75 mm; YMC, Japan) controlled at a column temperature of 40 °C. Samples were resolved on the column using a linear gradient of 50 to 100% acetonitrile for 12 min, followed by elution with 100% acetonitrile for 13 min at a flow rate of 1.5 ml/min. The metabolites were detected by UV at 265 nm.

Crystallization and X-ray Diffraction Studies—Purified Vdh-WT was concentrated to 20 mg/ml in 20 mM Tris-HCl, pH 7.5, and 0–0.2% PMβCD (for VD$_3$ complex) or 0–0.2% γCD (for 25(OH)VD$_3$ complex), using a centrifugal ultrafiltration device with a 30-kDa cutoff membrane (Millipore). Vdh-K1 was also concentrated to 20 mg/ml under the same conditions as Vdh-WT, but supplemented with 20 mM NaCl. For substrate complex formation, saturated VD$_3$/25(OH)VD$_3$ dissolved in dimethyl sulfoxide (∼100 mM) was added to each sample at the volume ratio 1:99, and incubated overnight at 4 °C. The crystallization conditions were screened with 96-well sitting-drop plates at 20 °C by the sparse matrix approach. Optimization of the hit conditions were carried out by the hanging-drop vapor diffusion technique in 24-well plates at 20 °C. Vdh-WT crystals were grown using reservoir solution containing 0.1 M BisTris, pH 7.5, 50 mM CaCl$_2$, 40–120 mM NaCl or KCl, and 32–40% PEG 400 or PEG 550 monomethyl ether or 20% PEG 1000. Vdh-K1 was crystallized using reservoir solution containing 0.1 M calcium acetate and 10–14% PEG 3350. Crystals were flash-cooled under a nitrogen gas stream at 100 K for x-ray diffraction studies. Prior to flash cooling, crystals of Vdh-K1 were short-soaked with cryoprotectant, which is the crystallization mother liquor supplemented with 20% glycerol. All diffraction data were collected at the Photon Factory (PF, Tsukuba, Japan), using the charge-coupled device detector (ADSC). The data were indexed, integrated, and merged using the HKL2000 program package (24). Vdh-WT was crystallized in two crystal forms: the trigonal crystals were obtained in space group $P3_1$ with unit cell parameters $a = b = 62$, $c = 99$ Å, both in the presence and absence of VD$_3$/25(OH)VD$_3$, and the orthorhom-

bic crystals were grown in space group $P2_12_12_1$ with unit cell parameters $a = 63.6$, $b = 65.8$, $c = 102.3$ Å in the presence of saturated 25(OH)VD$_3$. Vdh-K1 was crystallized in orthorhombic space group $P2_12_12_1$ with unit cell dimensions of $a = 77$, $b = 172$, $c = 189$ Å, both in the presence and absence of VD$_3$/25(OH)VD$_3$.

Structure Determination and Model Analysis—The structure of Vdh-WT in trigonal crystal form was determined by the molecular replacement method with the program AMoRe (25), using P450 EryF model fragments (PDB code 1JIN) (26) as search probes. The structures of Vdh-WT and Vdh-K1 in orthorhombic crystal forms were solved by molecular replacement with the program MOLREP (27), using the trigonal Vdh-WT structure as a search model. All models were refined using the program REFMAC5 (28), and were inspected and corrected in the graphic program COOT (29). A randomly selected 5% of the observed reflections were set aside for cross-validation analysis and used to monitor various refinement stage. VD$_3$ and 25(OH)VD$_3$ models in Vdh-K1 were built based on a $F_o − F_c$ difference Fourier map in COOT. Electron density for 25(OH)VD$_3$ is clear, whereas that for VD$_3$ is partly ambiguous due to the high mobility and high temperature factors. The validities of all substrate models were verified by calculating the simulated annealing $2F_o − F_c$ composite omit map with the program CNS 1.1 (30) (supplemental Fig. S4). The stereochemical qualities of the final refined models were assessed by the program PROCHECK (31). The x-ray data collection and refinement statistics are summarized in Table 1. Structure superposition and assessment of conformational changes with difference distance matrices were performed with the program SuperPose (32). Molecular drawings were prepared using the program PyMOL (33).

RESULTS

Spectroscopic Characterization of Vdh—The binding affinities of VD$_3$/25(OH)VD$_3$ to Vdh-WT and Vdh-K1 were examined by UV-visible spectroscopy (Fig. 2). A small amount of PMβCD or γCD were added to the assay mixture to dissolve VD$_3$ or 25(OH)VD$_3$, respectively (see "Experimental Procedures"). The absorption spectra of Vdh-WT showed a Soret peak at 420 nm both in the presence and absence of VD$_3$ and 25(OH)VD$_3$ (Fig. 2A). This indicates that Vdh-WT is not affected by substrate addition and the heme iron is present consistently in a water-coordinated low-spin state. In contrast to Vdh-WT, significant spectral changes were detected for Vdh-K1. Purified Vdh-K1 is present as a mixture of high-spin (Soret peak at ≈390 nm) and low-spin (Soret peak at ≈420 nm) states, and the ratio of high/low-spin states is very sensitive to the addition of CDs. Typically, Vdh-K1 is present primarily as a low-spin state in the presence of PMβCD, whereas it prefers a high-spin state in the presence of γCD. Spectral titration of Vdh-K1 with VD$_3$ showed a spectral shift from the low-spin to high-spin state, which is a typical substrate-binding spectral change (type I spectral change; Fig. 2B). Unexpectedly, spectral titration of Vdh-K1 with 25(OH)VD$_3$ produced a spectral shift from the high-spin (389 nm) to low-spin (414 nm) state (reverse type I spectral change), suggesting that an unidentified ligand is coordinated to the heme iron in the presence of 25(OH)VD$_3$
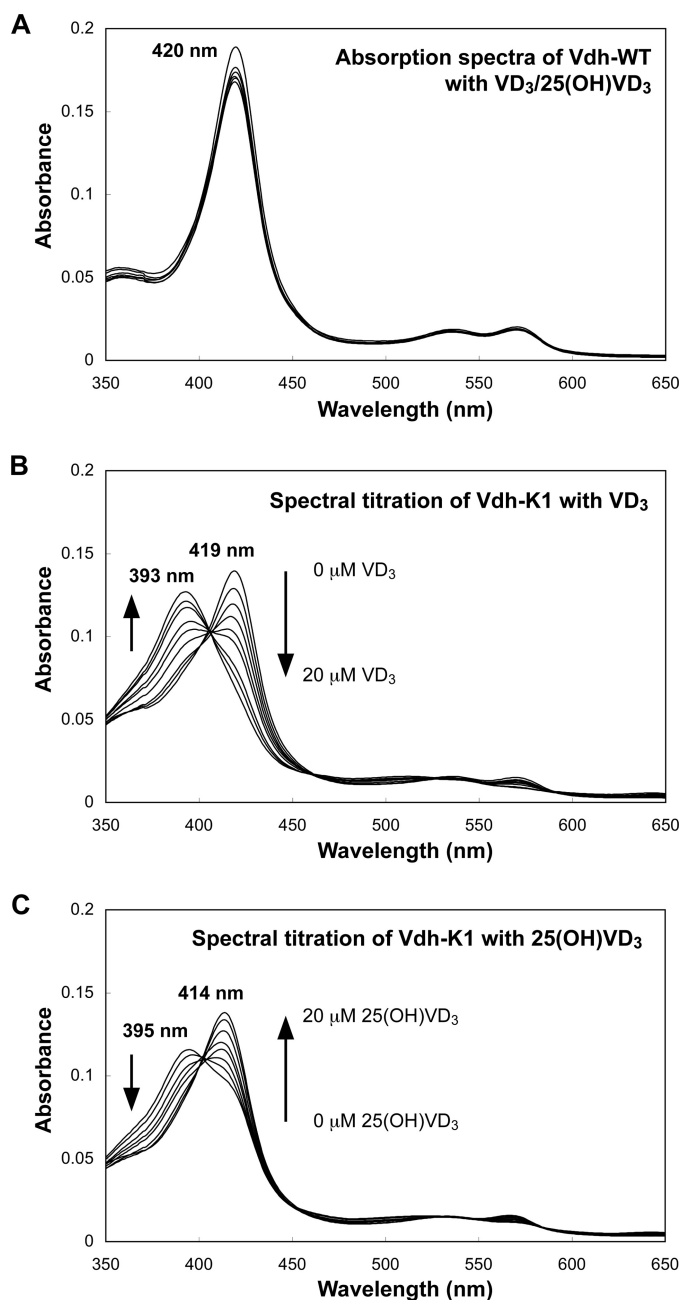
FIGURE 2. **Spectral changes of Vdh-WT and Vdh-K1 with VD$_3$/25(OH)VD$_3$.** UV-visible spectra for Vdh-WT on addition of 0, 10, and 20 μM VD$_3$/25(OH)VD$_3$ (*panel A*), and for Vdh-K1 on addition of 0–20 μM VD$_3$ (*panel B*) and 0–20 μM 25(OH)VD$_3$ (*panel C*). *Arrows* indicate the directions of spectral changes in response to the increase in VD$_3$/25(OH)VD$_3$ concentrations. Wavelength (nm) at maximum height of Soret band observed in each spectral measurement is also indicated.

(Fig. 2*C*). The ligand exhibiting the Soret peak at 414 nm was identified as the C3 OH group (3β-OH) of 25(OH)VD$_3$ by x-ray structure analysis, as described later.

General Description of Vdh Structure—The crystal structures of Vdh-WT in the substrate-free form and Vdh-K1 in both the substrate-free and substrate-bound forms were determined by molecular replacement using P450 EryF (CYP107A1) as a search model (Fig. 3 and Table 1). Molecules in all crystal forms have a well defined continuous electron density, except for several N-terminal residues and C-terminal His tag regions. The

overall structure of Vdh exhibits a typical triangular-shaped P450-fold consisting of 13 α-helices (A-helix to M-helix) and 8 β-strands (a-strand to h-strand). The heme cofactor is located at the center of the molecule and is sandwiched between distal I-helix and proximal L-helix. The heme propionate groups are tightly bound to side chains Arg[289], His[95], and His[345]. The thiol group of Cys[347] is coordinated to the heme iron, as shown in previously reported CYP structures. A sequence similarity search indicated that Vdh is a member of the family CYP107. The structures of three molecular species of CYP107 (EryF (26, 35, 36), PikC (37, 38), and BioI (39)) have been solved to date; a pairwise structure comparison revealed that Vdh is the most related to PikC (CYP107L1).

Vdh-WT Forms an Open Conformation—The crystal structure of Vdh-WT was determined in the substrate-free form at a resolution of 1.75 Å (Fig. 3). The asymmetric unit comprises one Vdh-WT monomer. Vdh-WT is most structurally related to substrate-free PikC in the open conformation (PDB code 2BVJ, chain B) (37) with a root mean square deviation (r.m.s. deviation) of 2.6 Å for 376 Cα atoms (supplemental Fig. S3). Differences in the main chain conformation are observed in two loop regions: an N-terminal loop (residues 10–17) and a loop between B-helix and C-helix commonly referred to as a "BC-loop" (residues 71–85). The BC-loop is known to be flexible and is partially disordered in the substrate-free PikC structure. The BC-loop in Vdh-WT protrudes from the globular body of the P450-fold, and the substrate-binding pocket on the distal side of the heme is widely open and exposed to the solvent (Fig. 3 and supplemental Fig. S5*A*). The water ligand is bound to the distal side of the heme iron with a Fe-O distance of 2.4 Å. Extra electron density is also observed in the large pocket mainly surrounded by hydrophobic residues, in which a model of polyethylene glycol (PEG) was reasonably fitted. The bound PEG is likely a crystallization artifact.

We also obtained crystals of Vdh-WT in the presence of substrates in two different forms. The same trigonal crystals were grown with saturated VD$_3$ or 25(OH)VD$_3$, but the structures were completely similar to that in the substrate-free open conformation. Vdh-WT also crystallized in the orthorhombic space group $P2_12_12_1$ with saturated 25(OH)VD$_3$, and the structure was determined at 3.05-Å resolution. The overall structure in the orthorhombic crystal also superposed very well onto that in trigonal form, including the BC-loop, with an r.m.s. deviation of 1.0 Å for 395 Cα atoms (supplemental Fig. S2*A*). In both structures, no electron density for VD$_3$/25(OH)VD$_3$ bound to the active-site pocket was observed. These results indicate that the open conformation of Vdh-WT is stable and not affected by crystal lattice forces, even in the presence of saturated VD$_3$/25(OH)VD$_3$.

Closed Structure of Vdh-K1 in Substrate-free and Substrate-bound Forms—The structures of Vdh-K1 in the substrate-free, VD$_3$-bound, and 25(OH)VD$_3$-bound forms were determined at 2.3-, 2.05-, and 2.0-Å resolutions, respectively (Fig. 3). Crystallization screening of Vdh-K1 yielded only one orthorhombic form with relatively large unit-cell dimensions compared with Vdh-WT crystals. The asymmetric unit contains 5 Vdh-K1 monomers that are not related by point-group symmetry. The structures of all the refined models of Vdh-K1 (15 monomers)

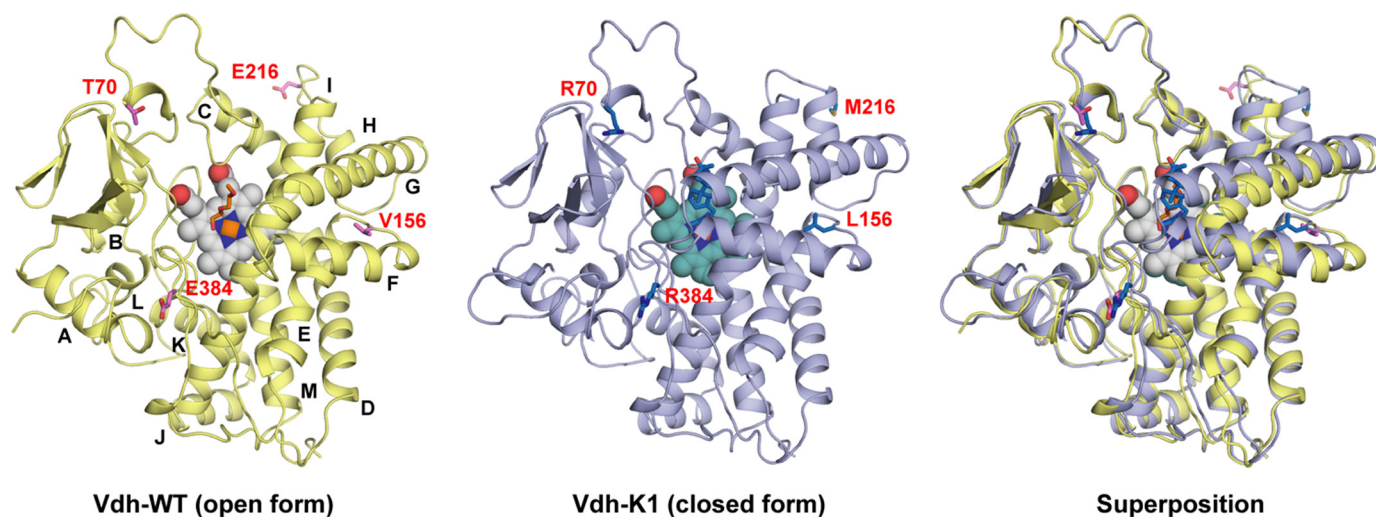**Vdh-WT (open form)**   **Vdh-K1 (closed form)**   **Superposition**

FIGURE 3. **Ribbon diagram of overall structure of Vdh-WT (open form) and Vdh-K1 (closed form).** Overlay of these two structures is also shown. The heme cofactor is in the *sphere*, and the bound-substrate (25(OH)VD$_3$) and the side chains of mutational residues at positions 70, 156, 216, and 384 are in *sticks*. The α-helices are labeled alphabetically from the N to C terminus.

TABLE 1

Crystallographic parameters and refinement statistics

	PDB code				
	3A4G	**3A4H**	**3A4Z**	**3A50**	**3A51**
Model	Vdh-WT	Vdh-WT	Vdh-K1	Vdh-K1	Vdh-K1
Conformation	Open	Open	Closed	Closed	Closed
No. monomers in the AU	1	1	5	5	5
Substrates	Substrate-free	Substrate-free	Substrate-free	VD$_3$	25(OH)VD$_3$
Data collection					
Beamline	PF-BL5A	PF-BL17A	AR-NE3A	AR-NE3A	AR-NW12A
Wavelength (Å)	1.0000	1.0000	1.0000	1.0000	1.0000
Space group	$P3_1$	$P2_12_12_1$	$P2_12_12_1$	$P2_12_12_1$	$P2_12_12_1$
Unit cell parameters (Å, deg)	61.7, 61.7, 98.8, 90, 90, 120	63.6, 65.8, 102.3, 90, 90, 90	77.4, 172.5, 189.9, 90, 90, 90	77.4, 172.3, 189.1, 90, 90, 90	77.2, 171.8, 189.1, 90, 90, 90
Resolution range (Å)[a]	50–1.75 (1.81–1.75)	50–3.05 (3.16–3.05)	50–2.20 (2.24–2.20)	50–2.05 (2.09–2.05)	50–2.00 (2.07–2.0)
Unique reflections	42,012	8,366	129,009	158,815	170,383
Redundancy[a]	5.3 (3.2)	3.6 (3.8)	7.3 (6.0)	7.5 (6.3)	7.4 (7.0)
Completeness (%)[a]	99.3 (93.2)	97.6 (97.9)	100.0 (99.8)	100.0 (99.8)	100.0 (100.0)
$I/\sigma (I)$[a]	21.9 (3.7)	18.9 (6.0)	26.0 (2.9)	26.9 (2.9)	32.5 (3.3)
R_{merge}[a,b]	0.075 (0.316)	0.090 (0.317)	0.101 (0.500)	0.107 (0.540)	0.077 (0.594)
Wilson B-factor (Å^2)	23.2	45.0	27.9	23.3	29.5
Refinement					
R_{work}/R_{free}[c]	0.185/0.236	0.217/0.270	0.201/0.244	0.201/0.240	0.197/0.234
R.m.s.deviation bond lengths (Å)	0.015	0.006	0.015	0.013	0.014
R.m.s.deviation bond angles (deg)	1.53	0.96	1.56	1.50	1.55
Total atoms	3,451	3,138	16,621	16,977	17,293
Average B-factors (Å^2)					
Overall	28.7	44.1	34.1	28.9	30.4
Ligands	35.3 (PEG)			69.0 (VD$_3$)	41.3 (25(OH)VD$_3$)
Ramachandran plot (%)	89.6/10.4/0.0/0.0	89.5/10.5/0.0/0.0	91.1/8.9/0.0/0.0	90.6/9.4/0.0/0.0	90.6/9.4/0.0/0.0

[a] Data for the highest resolution shell are provided in parentheses.
[b] $R_{merge} = \Sigma_h \Sigma_i |I_{h,i} - \langle I_h \rangle| / \Sigma_h \Sigma_i I_{h,i}$, where $\langle I_h \rangle$ is the mean intensity of a set of equivalent reflections.
[c] $R_{work} = \Sigma |F_{obs} - F_{calc}| / \Sigma F_{obs}$ for the 95% of the reflection data used in the refinement. F_{obs} and F_{calc} are observed and calculated structure factor amplitudes, respectively. R_{free} is the equivalent of R_{work}, except that it was calculated for a randomly chosen 5% test set excluded from the refinement.

are almost identical (r.m.s. deviation, < 0.7 Å), and no relatively large structural differences were observed, suggesting that the conformation of Vdh-K1 is also stable even in the substrate-free, VD$_3$-bound, and 25(OH)VD$_3$-bound states. Notably, local structural differences were found between Vdh-WT and Vdh-K1 (Figs. 3, 4, supplemental Fig. S2*B*, and Movies S1 and S2). The differences were most evident in the repositioning of the F- and G-helices, which are shifted by a distance of up to 8 Å, and the loop connecting the F- and G-helix (FG-loop) contacts the opposite loop (C-terminal loop) via two hydrogen bonds. This motion leads to a closed conformation where the substrate-binding pocket is covered by FG-helices (Figs. 3 and 4). An

additional conformational change occurs in a loop connecting H- and I-helix (HI-loop), and induces the extension of H-helix by 4 residues (Fig. 4). Similar conformational changes were also observed in the PikC structure, and Vdh-K1 is more structurally related to the closed form of PikC (PDB code 2BVJ, chain A; r.m.s. deviation of 3.0 Å for 378 Cα atoms) than to the open form of PikC (PDB code 2BVJ, chain B; r.m.s. deviation of 4.0 Å for 378 Cα atoms; supplemental Fig. S3) (37). The BC-loop is known to often move toward the substrate-binding pocket in response to substrate binding, whereas it is motionless in Vdh (Fig. 3). Therefore, the substrate-binding pocket is not fully closed and is partially accessible by the solvent. The four muta-
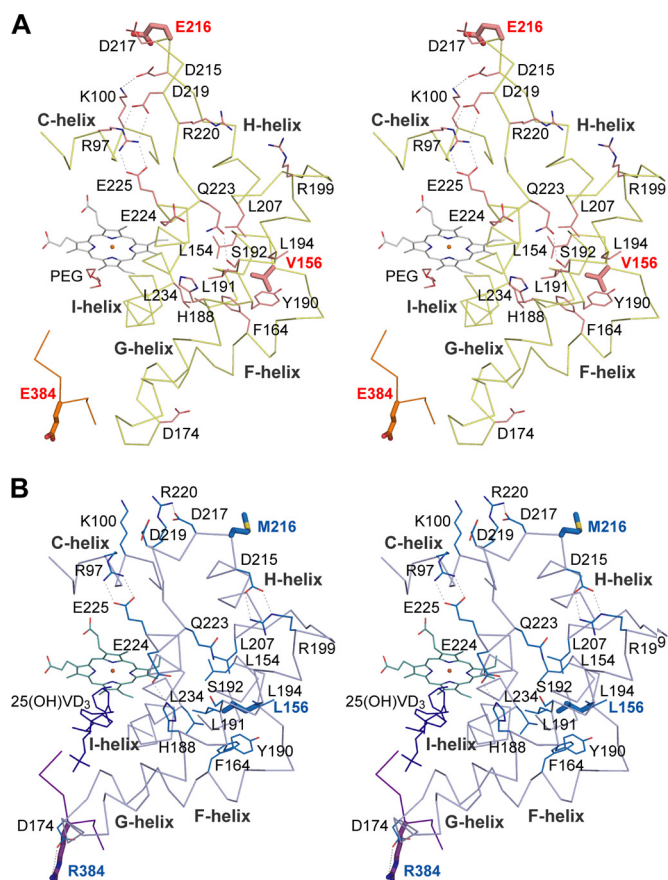
FIGURE 4. Stereo view Cα trace of the Vdh-WT (*panel A*) and Vdh-K1 (*panel B*) in the region composing C-, FG-, and HI-helices and the C-terminal loop. Mutational residues at positions 156, 216, and 384 are depicted in *sticks*. Salt bridges and hydrogen bonds broken and reconstituted during open/close motion are shown as *dashed lines*. Side chains involving these hydrophilic interactions or hydrophobic residues nearby Leu^{156}/Val^{156} creating hydrophobic core are in *thin sticks* and labeled.

tional positions in Vdh-K1 (T70R, V156L, E216M, and E384R) are not located at the substrate-binding site but are scattered throughout the molecule. We discuss later how these mutations are involved in the open/closed conformational change (see "Discussion").

VD$_3$ and 25(OH)VD$_3$ Are Bound to Vdh-K1 in an Anti-parallel Orientation—Vdh catalyzes the two-step hydroxylation of VD$_3$ to 1α,25(OH)$_2$VD$_3$ via 25(OH)VD$_3$. Because the hydroxylation positions are discrete, VD$_3$ and 25(OH)VD$_3$ must be bound in different orientations. The electron density shows that VD$_3$ is bound in an extended conformation at the active-site pocket, and the aliphatic side chain including C25 is located in the vicinity of the heme iron (Fig. 5, *A* and *B*). The mean distance between the C25 of VD$_3$ and the heme iron of each molecule is 4.6 ± 0.1 Å. No solvent is coordinated to the distal site of the heme iron probably due to VD$_3$ binding. These observations support the high-spin state of the heme iron as shown by spectroscopic data. The mean refined *B*-factor value for VD$_3$ atoms is 69 Å^2, suggesting that VD$_3$ is not tightly bound to the enzyme. Actually, the conformation of the five refined VD$_3$ models in each monomer is varied, especially in the A-ring moiety for which the electron density is even lower and unclear (Fig. 5, *A* and *B*, and supplemental Fig. S4). The aliphatic side chain

and the CD-rings of VD$_3$ are surrounded by hydrophobic side chain atoms of residues Met^{86}, Ile^{88}, Leu^{89}, Leu^{171}, Ile^{235}, Leu^{232}, Pro^{287}, and Leu^{387} with distances ranging from 3.6 to 4.5 Å, whereas the A-ring moiety is considerably exposed to the solvent (Fig. 5*B*). Although Trp^{67}, Pro^{83}, Lys^{180}, Asn^{181}, and Met^{184} derived from BC-loop, FG-loop, and G-helix lie near the A-ring, there are no specific interatomic interactions with a unique hydrophilic 3β-OH of A-ring. In contrast, the electron density for 25(OH)VD$_3$ is very clear, and it is evidently bound in an anti-parallel orientation (Fig. 5, *C* and *D*, and supplemental Fig. S4). The mean *B*-factor value for 25(OH)VD$_3$ atoms is 41 Å^2, which is lower than that for VD$_3$. The clear electron density also revealed that A-ring forms in a boat conformation with an axial 3β-OH occupying the sixth coordinate position of the heme iron with a mean distance of 2.5 ± 0.1 Å. The hydroxylating site C1 is located at a distance of 5.0 ± 0.0 Å from the heme iron. The 3β-OH coordination to the heme iron explains the Soret peak at 414 nm in the spectroscopic data. Unlike the A-ring of VD$_3$, the aliphatic side chain of 25(OH)VD$_3$ does not fluctuate even though it is partly exposed to the solvent and can be immobilized alongside of the FG-loop via van der Waals forces. In addition, in 4 of 5 molecules, hydrogen bonds form between 25-OH and one of the solvent molecules clustered at the entrance of the substrate-binding pocket; these also contribute to the attachment of the aliphatic side chain.

DISCUSSION

Interpretation of Spectroscopic Data—The absorption spectra of Vdh-WT show that the heme iron is present in a water-liganded low-spin state both in the presence and absence of a substrate (Fig. 2*A*). The crystal structures of Vdh-WT also reveals that no substrate is bound to Vdh-WT even in the presence of saturated VD$_3$/25(OH)VD$_3$. These results clearly show a very low substrate binding affinity despite the fact that the catalytic activity of Vdh-WT is comparable with those of physiologically VD$_3$-metabolizing CYP27A1 and CYP2R1 (2–4). One possible explanation is that substrate binding to Vdh-WT may occur depending on the association with a redox partner protein. Several cases have been reported to date where a redox protein functions as an effector that promotes substrate binding to CYPs (40, 41). In contrast to Vdh-WT, Vdh-K1 exhibits spectral changes in response to the addition of VD$_3$/25(OH)VD$_3$ (Fig. 2, *B* and *C*). The absorption peak in the Soret band is shown at 393 nm with VD$_3$ and at 414 nm with 25(OH)VD$_3$. The former clearly corresponds to a five-coordinate high-spin state of the heme iron caused by VD$_3$ binding, whereas the latter indicates a six-coordinate low-spin state. The structure of Vdh-K1 with bound 25(OH)VD$_3$ revealed that the 3β-OH group of 25(OH)VD$_3$ is a sixth coordination ligand that is positioned very close to the heme iron. Ligation of the OH group to the heme iron was previously reported in the structure of P450$_{cam}$ complexed with the product 5-*exo*-hydroxycamphor (42). In addition, several mammalian CYPs show the reverse type I spectral change in response to the addition of a substrate or inhibitor carrying OH groups (Ref. 43 and references therein). Obviously, the OH-bound heme iron reduces the catalytic activity of CYP, because the low-spin ferric state
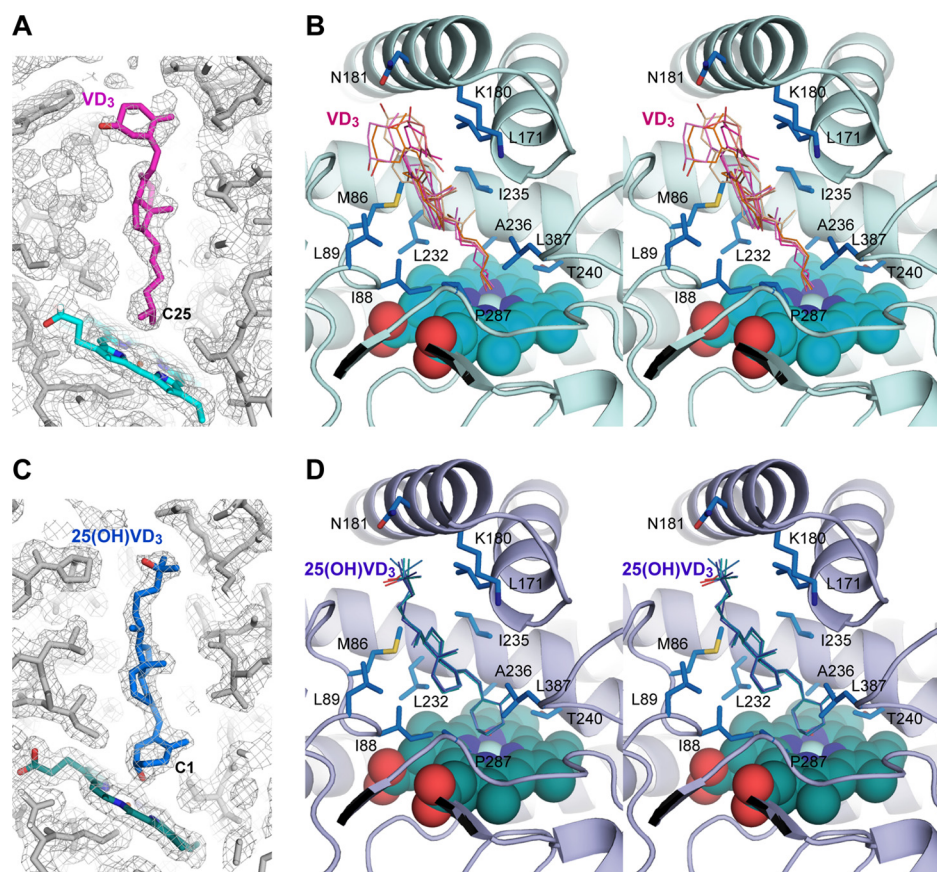
FIGURE 5. **VD₃ and 25(OH)VD₃ binding to Vdh-K1.** Final $2F_o - F_c$ electron density map for VD₃ (*panel A*) and 25(OH)VD₃ (*panel C*) contoured at 0.8σ level (chain ID, *A*). Unbiased simulated annealing composite omit map for all chains in the asymmetric unit are shown in supplemental Fig. S4. *B*, stereo view active-site structure with bound VD₃ in chain A. All five refined models of VD₃ in each chain in the asymmetric unit are superimposed and shown as *thin sticks*. Residues creating the substrate-binding pocket are shown in *sticks* and are labeled. The heme cofactor is the *sphere*. *D*, stereo view active site structure with bound 25(OH)VD₃ prepared in the same way and in the same orientation to *panel B*.

hydrophobic cluster formed by the side chains of Phe[164], Leu[191], Leu[194], Leu[154], Leu[207], and Tyr[190] (Fig. 4A). The substitution from Val to Leu gives rise to steric hindrance with the side chains Phe[164] and Tyr[190] in the open state, thus requiring the spatial repositioning of these hydrophobic side chains. In the Vdh-K1 structure, the hydrophobic cluster is actually rearranged by changing the torsion geometries of these side chains together with the approximately ~8-Å shift of FG-helices, and consequently, the interatomic distances are reoptimized (Fig. 4B). Glu[216] is located at the protrusive HI-loop, and its side chain is fully exposed to the solvent with a relatively high *B*-factor value (about 55 Å²) in the Vdh-WT structure. The solvent-exposed methionine is unfavorable for protein stability, and the E216M mutation possibly functions as a driving force for conformational change of the HI-loop and extension of H-helix involving Met[216]. It is of interest to note that several salt bridges and hydrogen bonds are broken and reconstructed between residues derived from the C-, FG-, and HI-helices region during the conformational change (Fig. 4). These rearrangements of interatomic interactions imply that motions in the FG- and HI-helices regions are mutually cooperative. In contrast, the two other mutations (E384R and T70R) lie in the structurally rigid region. Arg[384] is located at the C-terminal loop that interacts with the FG-loop in the closed Vdh-K1 structure. The main chain O of Arg[384] and side chain OH of Ser[385] form hydrogen bonds to the main chain N of Asp[174] and main chain O of Val[172] at the FG-loop, respectively. In addition, electrostatic interactions occur between the side chain guanidyl of Arg[384] and carboxyl of Asp[174] with distances of 3.5–5 Å (Fig. 4B). It is thus likely that substitution from acidic to basic residues at position 384 somewhat increases the stability of the closed conformation. It is unclear whether Arg[70] contributes to the conformational change and increase in substrate binding affinity. In several CYPs, arginine residues at the entrance of the substrate access channel are suggested to play a crucial role in substrate recognition and/or guiding substrate entry and egress (44, 45). Likewise, Arg[70] in Vdh-K1 is located at the entrance of the substrate-binding pocket and may provide a weak primary binding site that improves the efficiency of substrate entry and egress. To investigate which mutations contribute most to the conformational change, the absorption spectra of each single mutant (T70R, V156L, E216M, and E384R) were also mea-

with very low redox potential precludes its reduction of the heme iron that is needed for the subsequent electron transfer and dioxygen binding. Therefore, further repositioning of the A-ring of 25(OH)VD₃ would be required for promoting the reduction and monooxygenation at the C1α site.

The spectral data suggest that the binding affinities of both substrates to Vdh increase by directed evolution. The specific activity measurements also showed that Vdh-K1 is ~12 times more active for VD₃ 25-hydroxylation and 25 times more active for 25(OH)VD₃ 1α-hydroxylation than Vdh-WT (supplemental Table S1). The high binding affinity and catalytic activity of Vdh-K1 for 25(OH)VD₃ are totally unexpected, because we monitored only the VD₃ 25-hydroxylase activity in the directed evolution experiments. These results strongly suggest that the four mutations do not improve the substrate specificity but affect the underlying enzyme mechanisms that are common to both hydroxylation activities.

Structural Insights into Activity Enhancement by Directed Evolution—Current structural studies reveal that the conformational change from the open to closed state results from the four amino acid substitutions generated by directed evolution. Then the question arises as to how these individual mutations contribute to the conformational change. Val[156] lies at the loop connecting E- and F-helix, and its side chain is buried inside the

sured on addition of 0–20 μM substrates. As shown in supplemental Fig. S1, only the V156L mutant showed an obvious but relatively small substrate-induced spectral change, whereas no spectral changes were observed for three other mutants similar to Vdh-WT. The results suggest that the combination of these mutations is essential to elicit high substrate binding affinities observed in Vdh-K1.

Elaborate rearrangements of interatomic interactions around CFGHI helices imply that the closed structure observed in Vdh-K1 is not a novel conformational state that resulted from directed evolution but rather a naturally pre-existing state. The original residues at mutational positions seemingly cause no serious problems even in the closed conformation. Furthermore, open Vdh-WT and closed Vdh-K1 are structurally related to the naturally existing open and closed states of wild-type PikC (supplemental Fig. S3). Several CYPs are known to undergo conformational changes even in the absence of a substrate, and the substrate complex formation likely arises from a pre-existing conformational equilibrium rather than an induced fit mechanism (37, 46–48). In the present work, it is likely that the directed evolution was responsible for the shift in conformational equilibrium toward the closed conformation and facilitation of VD_3/25(OH)VD_3 binding. Vdh-WT may surmount an energy barrier and transform from the open to closed state in response to the native substrate binding, and the current Vdh-K1 structure may mimic the putative closed form of Vdh-WT when bound to the native substrate. Many CYPs show extremely broad substrate specificity, presumably involving an open/close motion (49). Typically, the open and closed structures correspond to the substrate-free and substrate-bound forms, respectively, and our results thus introduce the possibility that identification of mutational positions inducing a shift in conformational equilibrium toward the closed form would unselectively increase the substrate binding affinity and catalytic activities.

We observe a remarkable parallel between our directed evolution studies of Vdh and natural selection of CYP51 mutants identified in *Candida albicans* azole-resistant isolates that emerged under selective pressure of antifungal drug fluconazole (50). In both cases, substrate/inhibitor binding affinities are greatly influenced by mutations in remote loops. These mutations presumably play a role in orchestrating the conformational transition and enhancing the enzyme performance. The parallel suggests that the mechanism could be widely used in nature to adapt CYPs to ever-emerging new conditions and substrates.

Anti-parallel Substrate Binding Modes Enabling Sequential Hydroxylation—On the basis of spectroscopic and crystallographic data, it is strongly suggested that Vdh-K1 has an exactly specified binding orientation for each substrate. Intriguingly, the backbone and side chain conformations at the active-site pocket are identical among the substrate-free, VD_3-bound, and 25(OH)VD_3-bound forms of Vdh-K1, and no induced-fit mechanisms are observed, although VD_3 is asymmetric (Fig. 5). In light of these structural findings, it is likely that the binding orientation depends on simply whether the C25 site is hydroxylated. VD_3 is bound to the enzyme in an orientation that positions the aliphatic side chain containing C25 toward the heme

iron and the A-ring containing the hydrophilic 3β-OH group toward the entrance of the substrate-binding pocket exposed to the solvent (Fig. 5*B*). This binding orientation is possibly a consequence of the need to prevent exposure of the hydrophobic aliphatic side chain to the solvent, and is also consistent with the fact that Vdh exhibits only 25-hydroxylase activity against VD_3. Once C25 is hydroxylated, 25(OH)VD_3 is bound to the enzyme in an anti-parallel orientation with 3β-OH of A-ring anchored to the heme iron, thereby enabling the subsequent 1α-hydroxylation. The existence of two substrate binding modes in different orientations implies that Vdh-K1 is not functionally specialized.

In mammals, VD_3 is hydroxylated by mainly CYP27A1, CYP2R1, and CYP27B1. Of these CYPs, the crystal structure of CYP2R1 has been determined in complex with VD_3 (4). In CYP2R1, VD_3 is fully buried in the hydrophobic active site pocket, and the A-ring of VD_3 facing the protein surface is also surrounded and stabilized by hydrophobic interactions with several of the aromatic side chains (supplemental Fig. S5*D*). The well fitted substrate-bound form of CYP2R1 exemplifies the functionally specialized structure of a VD_3 25-hydroxylase. Recently, the structures of P450 SU-1 (CYP105A1) from *Streptomyces griseolus* have been reported, which is another example of bacterial CYP that is capable of hydroxylating VD_3 (34, 45). The product 1α,25(OH)$_2$$VD_3$ lies sideways within the large active site pocket of CYP105A1, and the hydroxylating sites, C25 and C1, are located at a distance of about 11 Å from the heme iron (supplemental Fig. S5*C*). The authors suggested that the 1α,25(OH)$_2$$VD_3$ binding site far from the heme iron is presumably a primary binding site, and the substrate would be required to move closer to the heme iron for a catalytic reaction (34, 45). These different VD_3 binding conditions give a glimpse into the impressive versatility of CYPs.

REFERENCES

1. Jones, G., Strugnell, S. A., and DeLuca, H. F. (1998) *Physiol. Rev.* **78,** 1193–1231
2. Prosser, D. E., and Jones, G. (2004) *Trends Biochem. Sci.* **29,** 664–673
3. Sawada, N., Sakaki, T., Ohta, M., and Inouye, K. (2000) *Biochem. Biophys. Res. Commun.* **273,** 977–984
4. Strushkevich, N., Usanov, S. A., Plotnikov, A. N., Jones, G., and Park, H. W. (2008) *J. Mol. Biol.* **380,** 95–106
5. Yamamoto, K., Uchida, E., Urushino, N., Sakaki, T., Kagawa, N., Sawada, N., Kamakura, M., Kato, S., Inouye, K., and Yamada, S. (2005) *J. Biol. Chem.* **280,** 30511–30516
6. Deeb, K. K., Trump, D. L., and Johnson, C. S. (2007) *Nat. Rev. Cancer* **7,** 684–700
7. Zhu, G. D., and Okamura, W. H. (1995) *Chem. Rev.* **95,** 1877–1952
8. Sasaki, J., Miyazaki, A., Saito, M., Adachi, T., Mizoue, K., Hanada, K., and Omura, S. (1992) *Appl. Microbiol. Biotechnol.* **38,** 152–157
9. Takeda, K., Asou, T., Matsuda, A., Kimura, K., Okamura, K., Okamoto, R., Sasaki, J., Adachi, T., and Omura, S. (1994) *J. Ferment. Bioeng.* **78,** 380–382
10. Fujii, Y., Kabumoto, H., Nishimura, K., Fujii, T., Yanai, S., Takeda, K., Tamura, N., Arisawa, A., and Tamura, T. (2009) *Biochem. Biophys. Res. Commun.* **385,** 170–175
11. Coon, M. J., Ding, X. X., Pernecky, S. J., and Vaz, A. D. (1992) *FASEB J.* **6,**

669–673

12. Denisov, I. G., Makris, T. M., Sligar, S. G., and Schlichting, I. (2005) *Chem. Rev.* **105,** 2253–2277

13. Julsing, M. K., Cornelissen, S., Buhler, B., and Schmid, A. (2008) *Curr. Opin. Chem. Biol.* **12,** 177–186

14. Gillam, E. M. J. (2008) *Chem. Res. Toxicol.* **21,** 220–231

15. Gillam, E. M. J. (2007) *Arch. Biochem. Biophys.* **464,** 176–186

16. Fasan, R., Meharenna, Y. T., Snow, C. D., Poulos, T. L., and Arnold, F. H. (2008) *J. Mol. Biol.* **383,** 1069–1080

17. Li, S., Chaulagain, M. R., Knauff, A. R., Podust, L. M., Montgomery, J., and Sherman, D. H. (2009) *Proc. Natl. Acad. Sci. U.S.A.* **106,** 18463–18468

18. Lewis, J. C., Bastian, S., Bennett, C. S., Fu, Y., Mitsuda, Y., Chen, M. M., Greenberg, W. A., Wong, C. H., and Arnold, F. H. (2009) *Proc. Natl. Acad. Sci. U.S.A.* **106,** 16550–16555

19. Mitani, Y., Meng, X., Kamagata, Y., and Tamura, T. (2005) *J. Bacteriol.* **187,** 2582–2591

20. Yasutake, Y., Fujii, Y., Cheon, W. K., Arisawa, A., and Tamura, T. (2009) *Acta Crystallogr. Sect. F Struct. Biol. Cryst. Commun.* **65,** 372–375

21. Omura, T., and Sato, R. (1964) *J. Biol. Chem.* **239,** 2370–2378

22. Hemsley, A., Arnheim, N., Toney, M. D., Cortopassi, G., and Galas, D. J. (1989) *Nucleic Acids Res.* **17,** 6545–6551

23. Villalonga, R., Cao, R., and Fragoso, A. (2007) *Chem. Rev.* **107,** 3088–3116

24. Otwinowski, Z., and Minor, W. (1997) *Methods Enzymol.* **276,** 307–326

25. Navaza, J. (1994) *Acta Crystallogr. Sect. A* **50,** 157–163

26. Cupp-Vickery, J. R., Garcia, C., Hofacre, A., and McGee-Estrada, K. (2001) *J. Mol. Biol.* **311,** 101–110

27. Vagin, A., and Teplyakov, A. (1997) *J. Appl. Crystallogr.* **30,** 1022–1025

28. Murshudov, G. N., Vagin, A. A., and Dodson, E. J. (1997) *Acta Crystallogr. D Biol. Crystallogr.* **53,** 240–255

29. Emsley, P., and Cowtan, K. (2004) *Acta Crystallogr. D Biol. Crystallogr.* **60,** 2126–2132

30. Brünger, A. T., Adams, P. D., Clore, G. M., DeLano, W. L., Gros, P., Grosse-Kunstleve, R. W., Jiang, J. S., Kuszewski, J., Nilges, M., Pannu, N. S., Read, R. J., Rice, L. M., Simonson, T., and Warren, G. L. (1998) *Acta Crystallogr. D Biol. Crystallogr.* **54,** 905–921

31. Laskowski, R. A., MacArthur, M. W., Moss, D. S., and Thornton, J. M. (1993) *J. Appl. Crystallogr.* **26,** 283–291

32. Maiti, R., Van Domselaar, G. H., Zhang, H., and Wishart, D. S. (2004) *Nucleic Acids Res.* **32,** W590–594

33. DeLano, W. L. (2002) *The PyMOL Molecular Graphics System*, DeLano Scientific LLC, Palo Alto, CA

34. Sugimoto, H., Shinkyo, R., Hayashi, K., Yoneda, S., Yamada, M., Kamakura, M., Ikushiro, S., Shiro, Y., and Sakaki, T. (2008) *Biochemistry* **47,** 4017–4027

35. Cupp-Vickery, J. R., and Poulos, T. L. (1995) *Nat. Struct. Biol.* **2,** 144–153

36. Cupp-Vickery, J., Anderson, R., and Hatziris, Z. (2000) *Proc. Natl. Acad. Sci. U.S.A.* **97,** 3050–3055

37. Sherman, D. H., Li, S., Yermalitskaya, L. V., Kim, Y., Smith, J. A., Waterman, M. R., and Podust, L. M. (2006) *J. Biol. Chem.* **281,** 26289–26297

38. Li, S., Ouellet, H., Sherman, D. H., and Podust, L. M. (2009) *J. Biol. Chem.* **284,** 5723–5730

39. Cryle, M. J., and Schlichting, I. (2008) *Proc. Natl. Acad. Sci. U.S.A.* **105,** 15696–15701

40. Schenkman, J. B., and Jansson, I. (2003) *Pharmacol. Ther.* **97,** 139–152

41. Tosha, T., Yoshioka, S., Takahashi, S., Ishimori, K., Shimada, H., and Morishima, I. (2003) *J. Biol. Chem.* **278,** 39809–39821

42. Li, H. Y., Narasimhulu, S., Havran, L. M., Winkler, J. D., and Poulos, T. L. (1995) *J. Am. Chem. Soc.* **117,** 6297–6299

43. Shimada, T., Tanaka, K., Takenaka, S., Foroozesh, M. K., Murayama, N., Yamazaki, H., Guengerich, F. P., and Komori, M. (2009) *Chem. Res. Toxicol.* **22,** 1325–1333

44. Winn, P. J., Lüdemann, S. K., Gauges, R., Lounnas, V., and Wade, R. C. (2002) *Proc. Natl. Acad. Sci. U.S.A.* **99,** 5361–5366

45. Hayashi, K., Sugimoto, H., Shinkyo, R., Yamada, M., Ikeda, S., Ikushiro, S., Kamakura, M., Shiro, Y., and Sakaki, T. (2008) *Biochemistry* **47,** 11964–11972

46. Savino, C., Montemiglio, L. C., Sciara, G., Miele, A. E., Kendrew, S. G., Jemth, P., Gianni, S., and Vallone, B. (2009) *J. Biol. Chem.* **284,** 29170–29179

47. Scott, E. E., He, Y. A., Wester, M. R., White, M. A., Chin, C. C., Halpert, J. R., Johnson, E. F., and Stout, C. D. (2003) *Proc. Natl. Acad. Sci. U.S.A.* **100,** 13196–13201

48. Huang, W. C., Westlake, A. C., Maréchal, J. D., Joyce, M. G., Moody, P. C., and Roberts, G. C. (2007) *J. Mol. Biol.* **373,** 633–651

49. Poulos, T. L. (2003) *Proc. Natl. Acad. Sci. U.S.A.* **100,** 13121–13122

50. Podust, L. M., Poulos, T. L., and Waterman, M. R. (2001) *Proc. Natl. Acad. Sci. U.S.A.* **98,** 3068–3073